Journal of ELECTRONIC MATERIALS, Vol. 48, No. 11, 2019
https://doi.org/10.1007/s11664-019-07568-x

FTIR and Mössbauer Spectroscopy Investigations of $Ag/Fe_xAl_{2-x}O_3$ Nanocomposites

M.H. MAHMOUD [1,2,3] and T.A. TAHA[1]

1.—Physics Department, College of Science and Arts, Jouf University, P.O. Box 756, Al-Gurayyat, Saudi Arabia. 2.—e-mail: mhissa@ju.edu.sa. 3.—e-mail: mohom63@yahoo.com

An investigation of Ag/(hematite-alumina) solid solutions ($Ag/Fe_xAl_{2-x}O_3$, $0.5 \le x \le 2$) was completed via x-ray diffraction (XRD), scanning electron microscopy (SEM), Fourier transform Infrared spectroscopy (FTIR) and Mössbauer spectroscopy. Results reveal that the materials obtained by combustion synthesis are multi-phase nanocomposites and silver metal is supported on hematite-rich and alumina-rich nanoparticles for $x < 2$. For the iron-rich hematite phase, the experimental results indicated a beginning transition to the superparamagnetic state. They also show that the distribution of iron and aluminum cations in the product phases strongly depends on the starting concentrations and that their compositions closely correspond to those of the equilibrium phase diagram at about 1250°C. Mössbauer signal intensities of samples with $x = 0.5$, 1.0 and 1.5 could consistently be explained by coexistence of phases of approximate composition $Fe_{0.2}Al_{1.8}O_3$ and $Fe_{1.8}Al_{0.2}O_3$, which closely corresponds to the thermodynamic equilibrium phase diagram of Fe_2O_3-Al_2O_3 at about 1250°C. Finally, the Mössbauer spectra reveal line shape changes for the samples with $x < 2$ which are characteristic for the onset of superparamagnetic behavior.

Key words: Ceramics, chemical synthesis, infrared spectroscopy, Mössbauer effect

INTRODUCTION

During the last few decades, metal and metal/oxide–ceramic composites have been extensively investigated due to their remarkable properties and application potential.[1–6] Iron-substituted alumina, which is a commonly employed sorbent and catalyst, has been the subject of various physicochemical investigations.[7–10] The main characteristics of alumina powders are surface acidity, mechanical resistance, high surface area and stability against sintering, as well as good insulating and diamagnetic properties. Among the materials that can be used as seed sources for the crystallization of the corundum structure of aluminum oxide, α-Fe_2O_3 appears to be one of the best choices because of it is isostructural with α-Al_2O_3 (space group $R\bar{3}c$, No. 167) with a close-packed oxygen lattice and Fe^{3+} cations located in octahedral sites.[11–14] However, the lattice dimension and molar volumes of the two compounds differ significantly: the hexagonal lattice constants of α-Al_2O_3 are given by a = 475.8 pm and c = 1299.1 pm and those of α-Fe_2O_3 by a = 503.4 pm and c = 1375.2 pm, yielding molar volumes of $V_m(Al_2O_3) = 25.6$ cm^3 and $V_m(Fe_2O_3) = 30.3$ cm^3, respectively.[15] Hematite (α-Fe_2O_3) is a complex magnetic material that is antiferromagnetic (AF) at low-temperatures. Above the so-called Morin temperature (TM = 260 K), it undergoes a transition to a weak ferromagnetic state (WF) because of spin canting.[16] The main characteristics of iron oxide powders are easy sintering as well as semiconducting and ferri- or antiferromagnetic properties. In principle, chemical mixing of α-Fe_2O_3 with α-Al_2O_3 could be beneficial to produce oxidation catalysts with improved stability

(Received May 8, 2019; accepted August 16, 2019; published online August 26, 2019)

or of mechanically and thermally stable redox-active powder materials.

Many papers have reported on the catalytic properties of the mixed oxide system Fe_2O_3-Al_2O_3. Mimura and Saito [17] reported high catalytic activity of Fe_2O_3 (10 wt.%)/Al_2O_3(90 wt.%) in the dehydrogenation of ethylbenzene to produce styrene in the presence of CO_2. Giecko et al.[18] tested the activity of Fe_2O_3 supported on Al_2O_3 towards the decomposition of nitrous oxide to remove N_2O from a nitric acid plant simulated process stream. The tested catalysts characterized by high activity (95% conversion of N_2O at 750°C), excellent mechanical stability and no decomposition of nitric oxide. The catalytic activity of the Fe_2O_3-Al_2O_3 system is greatly influenced by the addition of other components. In this way, it is found that doping Fe_2O_3-Al_2O_3 with Au and Mn_2O_3 (calcined at 300, 500 and 700°C) is accompanied by a progressive increase in catalytic activity of the investigated solid catalysts for CO oxidation by decomposition of O_2 and H_2O_2.[19] More recently, it was reported that the addition of Sn to Pt/Fe_2O_3-Al_2O_3 improved the isobutane dehydrogenation activity.[19] This catalyst revealed even better activity than that of the commercial Pt-Sn/Zn-Al-O catalyst, which is commonly employed in dehydrogenation reactions.[20] The addition of silver component to Fe_2O_3-Al_2O_3 enhanced the catalytic properties and, indeed, Ag/$Fe_xAl_{2-x}O_3$ nanocomposites already have been used successfully as catalysts in the decomposition of H_2O_2 and N_2O.[21] The activity of these catalysts influenced by the particle size of silver and the iron content in the catalyst.

Mössbauer spectroscopy is a powerful technique for analysing Fe-containing alloys and compounds, see e.g. Ref. 22 Moreover, Mössbauer spectroscopy (MS) can also detect phases that are difficult to differentiate by XRD because of their similar crystal structures, such as γ-Fe_2O_3 and Fe_3O_4. It also offers the possibility to observe magnetic transitions through the evolution of magnetic hyperfine fields and/or characteristic spectral line shapes. Furthermore, MS allows for the study of structural and electronic properties through isomer shifts and quadrupolar interactions. These hyperfine parameters give valuable information regarding the bonding environment and the symmetry of local structure around the Fe atoms. Therefore, as an extension of our previous work,[21] the main goal of the present study was to shed light onto the formation process of the catalytically active Ag/$Fe_xAl_{2-x}O_3$ nanocomposites and to analyze the solid-state reaction kinetics, possible phase transformations and the distribution of cations in the product phases as well as the magnetic state of the Ag/(α-Fe_2O_3–α-Al_2O_3) system obtained by the present synthetic conditions (combustion synthesis; annealing at 700°C followed by ignition) by using x-ray diffraction, SEM, FTIR and Mössbauer spectroscopy.

EXPERIMENTAL

All chemicals employed for synthesis ($AgNO_3$, $Fe(NO_3)_3{\cdot}9H_2O$, $Al(NO_3)_3{\cdot}9H_2O$ and CH_4N_2O) are analytical grade chemicals. Four mixtures of the general formula $Ag/Fe_xAl_{2-x}O_3$ (x = 0.5, 1.0, 1.5 and 2.0) were prepared using urea as combustion fuel. The amount of urea added during each preparation was 75% larger than the stoichiometric amount, i.e. the amount corresponding to complete combustion of urea and the nitrate anions in the parent mixtures.[21] The stoichiometric amounts of the reactant precursors were dissolved in distilled water, and kept in an oven at 90°C till a viscous gel was obtained. Finally, small portions of the obtained gel were calcined at about 700°C for 3 h in air and subsequently quenched to room temperature. During the first few minutes of the calcination process, ignition occurred with rapid evolution of a large amount of gases. Generally, the entire procedure was conducted with minimal exposure to light.

X-ray powder diffraction patterns were recorded using a Philips diffractometer (PW 103/00) operated at 35 kV and 20 mA providing Co-$K\alpha$ radiation. Scanning electron micrographs obtained using a JEOL scanning microscope (JSM-5400 LV). The infrared patterns recorded by means of a Thermo-Nicolet-6700 FTIR spectrophotometer using the KBr pellet technique in the range from $cm^{-1}$to 4000 cm^{-1}. ^{57}Fe Mössbauer spectroscopic measurements of the samples completed via a conventional microcomputer controlled spectrometer using a ^{57}Co/Rh radiation source. They were fitted with the *Recoil* Mössbauer spectral analysis software [23] and decomposed into sub-spectra with parameters of the following meaning: isomer shift IS (mm/s, relative to α-Fe at room temperature), half width Γ of the lines (mm/s), quadrupole splitting QS (mm/s), internal magnetic field B (T) and its distribution width ΔB (T), and relative spectral area A (%) of the individual sub-spectra.

RESULTS AND DISCUSSION

The phase changes accompanying the variation in the x-values of the $Ag/Fe_xAl_{2-x}O_3$ ($0.5 \le x \le 2$) system are checked by x-ray diffraction analysis (XRD). As shown in Fig. 1, it is found that the three phases Ag, an α-Al_2O_3- and an α-Fe_2O_3-type phase are present in the samples. Increasing x-values accompanied by a continuous decrease of the reflections characterizing the alumina-rich phase and by a continuous development of reflections due to the hematite-rich phase. The formation of silver metal—and not that of other possible phases such as Ag_2O, $AgFeO_2$ or $AgAlO_2$—appears to be a direct response of the present synthesis conditions using urea in excess as a reducing combustion fuel. In other words, employing urea as a combustion fuel favors the production of supported silver metal instead of silver containing oxides. It is to be noted, however, that Ag_2O decomposes at low

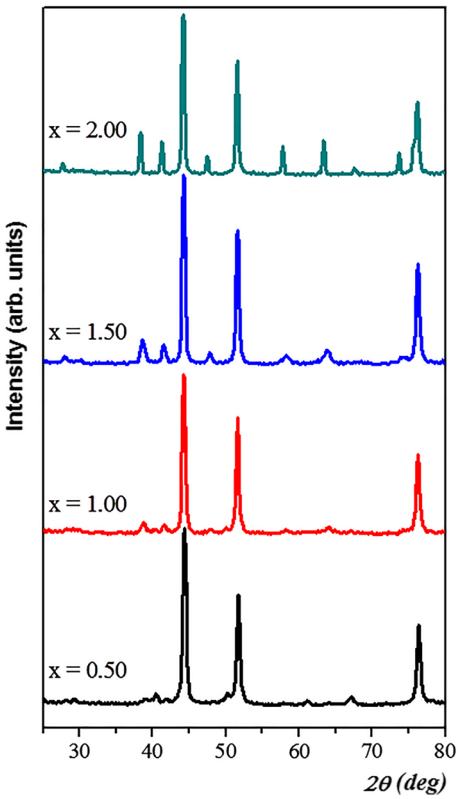

Fig. 1. XRD patterns of $Ag/Fe_xAl_{2-x}O_3$ nanocomposites ($0.5 \le x \le 2.00$).

Table I. The elemental nominal composition of the $Ag/Fe_xAl_{2-x}O_3$ nanocomposites

x	Al-nitrate (g)	Fe-nitrate (g)	Ag-nitrate (g)
0.50	12.12	4.35	7.32
1.00	7.76	8.36	7.02
1.50	3.73	12.06	6.76
2.00		15.48	6.51

temperatures and that the decomposition of the ternary $AgFeO_2$ phase is already occurring at temperatures of about 635°C.[24]

Average crystallite sizes, L_w, of silver metal and iron oxide are estimated from x-ray line width broadening by means of the Scherrer equation[25]:

$$\beta = \frac{k\lambda}{L_w \cos\theta} \quad (1)$$

Here, k is the Scherrer constant taken as 0.94,[26] λ is the x-ray wavelength and β is the corrected peak width. In these experiments, the width is taken as the full width at half maximum intensity of the peaks in the range $2\theta = 25°–80°$. The obtained values are listed in Table I. Inspection of Table I reveals that the crystallite size of Ag is approximately the same for all the samples (about 33 nm) irrespective of the iron content. On the other hand, the crystallite size of the Fe_2O_3-rich phase in the mixed system ($0.5 \le x \le 1.5$) amounts to about 13–16 nm and it is only for the pure hematite phase ($x = 2$) that a largely increased crystallite size of 36 nm is observed. Unfortunately, due to overlap of lines from metallic silver, no reliable data can be obtained for the alumina-rich phase. Nevertheless, these results confirm that the materials synthesized in the present work represent true nanocomposites. The elemental nominal composition of the $Ag/Fe_xAl_{2-x}O_3$ nanocomposites are given in Table I.

Based on the XRD analysis, SEM investigations were carried out for two concentrations ($x = 0.5$ and $x = 2$). As seen in Fig. 2, the sample with $x = 0.5$, Fig. 2a, consists of near-spherical crystallites with sizes varying in the 100–250 nm range. Moreover, irregularly distributed holes among the particles are evident. The average grain size of the catalyst with the higher iron content of $x = 2$, Fig. 2b, is larger with values varying in the 200–350 nm range. Comparison with the results obtained from XRD also shows that the particles seen in the SEM micrographs represent aggregates of nanoparticles. Moreover, the observed increase in the particles size accompanying the increasing x-values goes in parallel with the increase in the crystallite size of the iron-rich phase (Table II).

The FTIR spectra of the $Ag/Fe_xAl_{2-x}O_3$ nanocomposites ($0.5 \le x \le 2.00$) are reported in Fig. 3. As seen, the spectra of all samples showed the presence of an intense broad band in the high wave number range at about 3420 cm^{-1}, which can be assigned to stretching modes of OH groups of H_2O molecules.[27,28] The spectrum obtained for the $Ag/Fe_{0.5}Al_{1.5}O_3$ sample reveals the presence of additional absorptions bands at 640 cm^{-1}, 590 cm^{-1} and 446 cm^{-1}. However, the band at about 640 cm^{-1} is no longer visible in the $Ag/FeAlO_3$ sample with x = 1 and in samples with higher iron content. The further increase in the x-value to $x = 2.00$ is accompanied by a noticeable shift of the 590 cm^{-1} band to 559 cm^{-1} and of that originally (for $x = 0.5$) at 446 cm^{-1} to 474 cm^{-1}.

From the observed trend in these spectra the band at 640 cm^{-1} can be assigned to vibrational modes involving Al-O bonds,[29] which disappear with increasing x-values, i.e. with increasing Fe_2O_3 concentration. Concurrently, Okuno et al.[30] have observed a similar trend for $(SiO_2)_{1-x}(Al_2O_3)_x$ glass. The authors observed that with increasing Al_2O_3 content the relative intensity of a band at 400–500 cm^{-1}, assigned to Si-O-Si bending vibrations, decreases while that of a band at 500–900 cm^{-1}, assigned to the Al-O bond vibration, increases.

It is known that the position of IR bands of α-Fe_2O_3 as well as their relative intensities and broadening influenced by various parameters including the degree of crystallinity, grain morphology and the aggregation of particles besides their shape.[31,32] In this way for example, α-Fe_2O_3 spheres showed IR bands at 575 cm^{-1} and 485 cm^{-1},

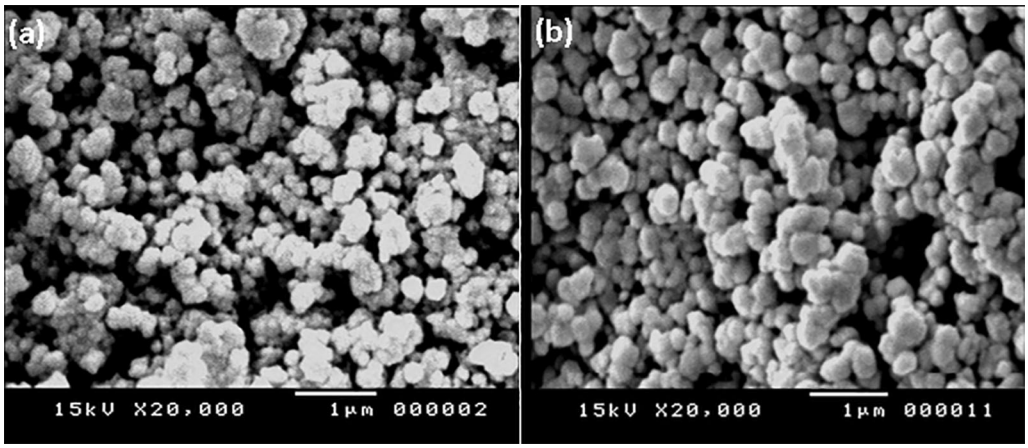

Fig. 2. SEM micrographs of (a) $Ag/Fe_{0.5}Al_{1.5}O_3$ and (b) Ag/Fe_2O_3 nanocomposites.

Table II. Crystallite sizes for Ag and the α-Fe_2O_3-rich phase ($0.5 \le x \le 2.00$) determined from XRD of the $Ag/Fe_xAl_{2-x}O_3$ nanocomposites

x	Ag (nm)	α-Fe_2O_3-type phase (nm)
0.50	31.2	13.2
1.00	33.4	12.8
1.50	34.2	16.0
2.00	32.5	36.2

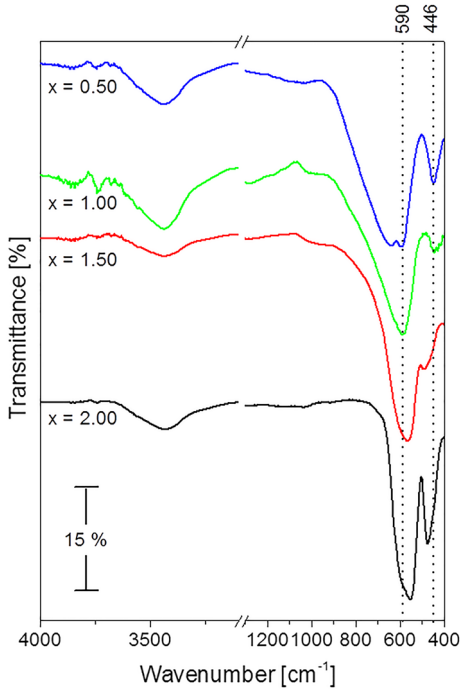

Fig. 3. FTIR spectra of $Ag/Fe_xAl_{2-x}O_3$ nanocomposites ($0.5 \le x \le 2.00$).

whereas α-Fe_2O_3 laths showed IR bands at 525 cm^{-1} and 440 cm^{-1}.[33] On the other hand, Ristić and Musić [34] found a very strong and broad band at

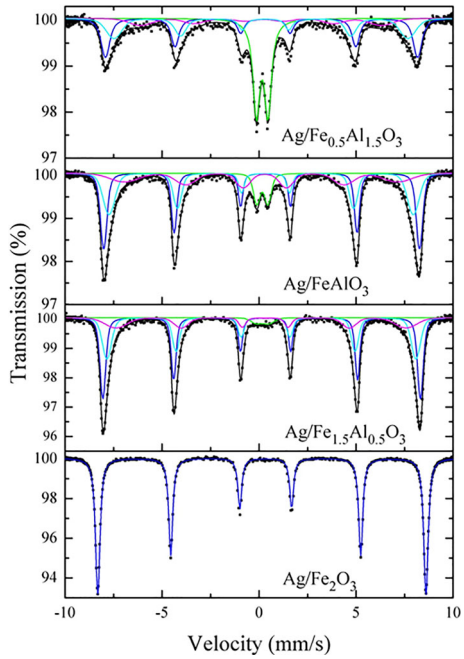

Fig. 4. ^{57}Fe Mössbauer spectra of $Ag/Fe_xAl_{2-x}O_3$ nanocomposites ($0.5 \le x \le 2.00$).

547 cm^{-1} with a shoulder at 596 and other bands at around 460 cm^{-1} for (porous) spheres of α-Fe_2O_3. Wang et al.[35] reported bands at 575 cm^{-1} and 484 cm^{-1} for α-Fe_2O_3 pseudo-cubes. Accordingly, it is reasonable to relate the two bands observed in Fig. 2 at 590 cm^{-1} and 446 cm^{-1}, which shift with increasing x-values to 559 cm^{-1} and 474 cm^{-1} to vibrational modes of the α-Fe_2O_3-rich phase.

Mössbauer spectra completed at room temperature for the samples with different iron content are shown in Fig. 4. The solid lines through the data points represent least-squares fits to the spectra. For $x = 2$ (Ag/Fe_2O_3), the observation of a magnetically split sextet with narrow lines shows that iron is magnetically ordered. The Mössbauer spectrum of any sample can be fitted by a single sextet of

Lorentzian line shape. The isomer shift of the sextet is typical for octahedrally coordinated high-spin Fe^{3+}.[36] The results of the spectral fit showed that the signal is almost identical to that of pure bulk hematite (α-Fe_2O_3) with a local magnetic field of 51.5 T, see Table III.[37] Detailed consideration of the central part of the spectrum also reveals that any possible additional signal contribution in this range must be clearly less than 1% of the total signal intensity. This allows the conclusion to be drawn that silver does not enter the hematite structure to any noticeable extent and that silver metal—in agreement with the results from XRD—is supported on the hematite-alumina system.

With decreasing iron content ($x < 2$), a doublet structure develops in the center of the Mössbauer spectra which then can be described by a superposition of a doublet and a magnetically split subspectrum. It is also observed that the magnetically split part of the spectrum with decreasing iron content develops progressively wider and more asymmetric lines. This magnetic part of the spectra can effectively be described by superposition of three magnetic subspectra (subspectra 1–3 in Table III) with isomer shifts which all are typical for octahedrally coordinated high-spin Fe^{3+} and local magnetic fields typical for octahedrally coordinated magnetically ordered high-spin Fe^{3+}, Table III. As seen, the local magnetic fields of these three magnetic subspectra decrease systematically with decreasing iron content. For subspectrum 1, for example, from 51.6 T ($x = 2$) to 49.7 T ($x = 0.5$) and similarly for subspectra 2 and 3 to magnetic fields as low as 38 T. In parallel, the fraction of iron giving rise to subspectrum 1 decrease from 100% for $x = 2$ to about 31% for the nanocomposite with $x = 0.5$ because of the line shape changes. On the other hand, with increasing alumina content, the quadrupole doublet (subspectrum 4 in Table III) at the center of the spectrum increases in intensity from zero for $x = 2$ to about 30% for $x = 0.5$. Its isomer shift is typical for high-spin Fe^{3+}, too. The quadrupole splitting (QS) of the doublet takes values of about 0.6 mm/s and apparently does not depend significantly on sample composition.

According to the equilibrium phase diagram of Fe_2O_3-Al_2O_3,[38–41] below about 1300°C the system is two-phase consisting of an alumina-rich and of a hematite-rich solid solution. It has been reported that—depending on temperature (1000–1300 C° in air)—the former phase can take up between 5 mol.% and 10 mol.% Fe_2O_3 ($0.1 \lesssim x' \lesssim 0.2$) and the hematite-rich solid solution can contain between about 8 and 20 mol.% of alumina ($1.6 \lesssim x'' \lesssim 1.85$). The reported miscibility gaps, thus, vary from almost symmetric, e.g. Ref. 38 to significantly asymmetric, e.g. $x' \approx 0.2$ and $x'' \approx 1.6$[40,41]; note that x is defined here as $x = 2{\cdot}n_{Fe}(n_{Fe} + n_{Al})$. Thus, at given temperature, for all total compositions x of $Fe_xAl_{2-x}O_3$ between x' and x'', two solid solution phases of composition x' and x'' are in equilibrium—if such conditions are prevailing. The two phases are isostructural, but differ considerably in lattice parameters.[15,38] Because of the high temperatures which are most probably reached in the sample preparation due to ignition of the reactive gel, it is accepted to assume that the $Ag/Fe_xAg_{2-x}O_3$ system decomposed into two alumina-hematite solid solutions plus Ag. This agrees with previous work [21]

Table III. ^{57}Fe Mössbauer spectra of $Ag/Fe_xAl_{2-x}O_3$ at room temperature: isomer shifts IS of subspectra, quadrupole perturbation ε_s of the magnetic spectrum and quadrupole splitting QS of paramagnetic doublet, line width Γ of subspectra, internal magnetic hyperfine fields B, widths of magnetic field distribution ΔB, and areas of the subspectra

Sample	Subsp.	IS (mm/s)	ε, QS (mm/s)	Γ (mm/s)	B (T)	ΔB (T)	Area (%)
$Ag/Fe_{0.5}Al_{1.5}O_3$	1	0.34	− 0.10	0.208	49.66	0.61	31.1
	2	0.32	− 0.12	0.208	46.99	1.89	25.3
	3	0.29	− 0.075	0.208	38.51	1.91	12.5
	4	0.27	0.59		–	–	31.1
$Ag/FeAlO_3$	1	0.34	− 0.10	0.099	50.47	0.65	37.7
	2	0.33	− 0.11	0.099	48.64	1.54	32.0
	3	0.31	− 0.1	0.099	43.72	3.90	22.5
	4	0.28	0.57	0.141	–	–	7.8
$Ag/Fe_{1.5}Al_{0.5}O_3$	1	0.35	− 0.102	0.097	50.74	0.56	45
	2	0.34	− 0.107	0.097	49.38	1.01	34
	3	0.32	− 0.109	0.097	46.37	3.16	18.2
	4	0.30	0.68	0.416	–		2.7 (8)
Ag/Fe_2O_3	1	0.35	− 0.099(2)	0.122(3)	51.59(1)		100
α-Fe_2O_3		0.38	− 0.21		51.5		Ref. 37

The isomer shifts are relative to α-Fe.

and the present XRD results obtained for the samples.

Thus, the magnetic sextets in the Mössbauer spectra are assigned to the hematite-type solid solution due to the high concentration of Fe^{3+} ions and, therefore, prevailing magnetic interactions. On the other hand, due to the lack of such interactions, the paramagnetic quadrupole doublet is associated with the alumina-type solid solution. Ladavos and Baka[42] studied the Mössbauer spectra of the system Fe_2O_3-Al_2O_3. For $x < 2$, they also observed a Mössbauer spectrum that is due to superposition of a sextet and a doublet (QS = 0.58 mm/s). However, their sextet for $x < 2$ is only given by one magnetic sextet and not—as in the present case—by superposition of several sextets with significantly different local magnetic field. Because the samples of the latter study prepared at 1150°C by annealing for extended times it is reasonable to assume that the product powders do not represent nanomaterials. Cordier et al.[43] in their study of the α-$Fe_{0.2}Al_{1.8}O_3$ solid solution observed a dominating doublet with a quadrupolar splitting of 0.54 mm/s and concluded that the sample's composition is very close to the solubility limit of ferric cations in the alumina phase. Mössbauer spectra of considerable complexity have been observed for materials obtained by mechanical ball milling of α-Fe_2O_3/α-Al_2O_3 mixtures, see e.g..[44] Many of the spectra exhibit line shape changes evidencing the beginning of superparamgnetic behavior of the material because of the small crystallite sizes reached by the mechanical processing.

Generally, if the grain size of a magnetic iron containing solid becomes smaller than acritical value D_c, sextets will gradually collapse and a so-called superparamagnetic doublet may appear. The critical grain size D_c of α-Fe_2O_3 is known to amount to about 20 nm at room temperature.[45,46] According to the preceding determination from the XRD data (Table I), the average crystallite size of about 15 nm for the α-Fe_2O_3-type solution phase is smaller than this critical value. Therefore, the appearance of superparamagnetic line shape changes is to be expected. Indeed, the peculiar development of line shapes of the magnetic spectra with their increasingly asymmetric lines—especially at their insides—represents a characteristic feature of an increasing influence of superparamagnetism and provides evidence for the onset of the underlying microscopic spin dynamics. An interesting question arises here as to the influence of the increasing spin dynamics on catalytic properties when the hematite-type solid solution transfers into the fully superparamagnetic state. On the other hand, the crystallite size of the Ag/Fe_2O_3 hematite sample ($x = 2$) is larger than D_c and, therefore, a narrow Lorentzian line shape is observed.

In further probing into the nature of the two subspectra of different type and into the distribution of cations in the two phases, Fig. 5 shows the

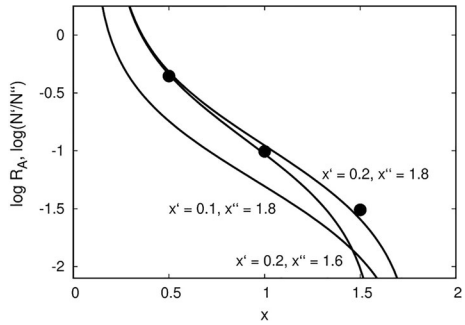

Fig. 5. Distribution of ferric ions in the two coexisting $Fe_xAl_{2-x}O_3$ nanophases ($x = 0.5$, 1.0, and 1.5). Data point for area ratio A_2/A_6 according to Table III. Lines drawn for different compositions x' and x'' of alumina-rich and hematite-rich phases, respectively, according to modified lever-rule.

area ratio of the doublet (A_2) and sextet (A_6) for the three samples ($x = 0.5$, 1.0, and 1.5) from the two-phase region of the phase diagram. A_2/A_6 corresponds to the respective ratio $N(Fe_{alu})/N(Fe_{hem})$ of the amount of ferric ions in the two phases. On the other hand, $N(Fe_{alu})/N(Fe_{hem})$ is closely related to the overall composition x of samples and to that of the coexisting phases by $N(Fe_{alu})/N(Fe_{hem}) = x'(x'' - x)/x''(x - x')$. The lines shown in Fig. 5 represent results obtained from the modified lever-rule for different solubility limits x' and x''. As seen, the present Mössbauer data are in good agreement with an almost symmetric solubility gap with $x' = 0.2$ and $x'' = 1.8$ as has been reported by Muan and Gee.[38] This clearly confirms the identification of doublet and sextet as being due to iron in the iron-poor alumina and iron-rich hematite phases. Comparing with the data of Ref. 38 it is concluded that the present samples possess a cation distribution and composition of product phases which closely corresponds to those of the equilibrium phase diagram at about 1250°C—even though crystallite sizes correspond to the nanoscale. This surprising result is attributed to the synthesis route employed in Ref. 21 and in the present study where urea is used in excess as combustion fuel of a reactive gel. Obviously, ignition of the gel provides the high temperatures necessary for cation transport to achieve the observed phase separation with close to equilibrium cation concentrations.

The solid state reaction leading to the present two-phase oxide nanosystem represents a complex problem of phase change with a moving boundary. Thus, any further discussion of the reactive processes should make numerous assumptions on idealized conditions for nucleation and growth of the nanophases. In addition to that, information on diffusion processes in the system Fe_2O_3-Al_2O_3 is scarce—even for the pure end members. We observed only a single temperature-dependent study of Al tracer diffusion in single crystalline α-Al_2O_3. For 1250°C, the data of Fielitz et al.[47] indicate a ^{26}Al diffusion coefficient of $7.7 \cdot 10^{-15}$ $cm^2 s^{-1}$. This is much smaller than the tracer

diffusion coefficient of ^{59}Fe in α-Fe_2O_3 of $2.7{\cdot}10^{-11}$ cm^2s^{-1} reported, e.g., by Hoshino and Peterson [48] for this temperature. We are not aware of any data on iron and/or aluminium diffusion in Fe_2O_3-Al_2O_3 solid solutions. Nevertheless, anticipating coupled diffusion of Al and Fe and that $D_{Al} \ll D_{Fe}$, effective diffusion coefficients will be determined by slow Al diffusion which in turn will determine the growth kinetics of the precipitate particles. It also appears realistic to expect that Al diffusion will increase with increasing iron content of the solid solutions. Thus, the above self-diffusion coefficient of Al can be considered a lower limit for any effective bulk diffusion coefficient in the system.

As mentioned, only a simple scenario of diffusion-controlled particle growth can be considered here. Such a model for diffusion-controlled growth of precipitate particles has been reported by Wert and Zener.[49] The model treats the growth of a fixed number of n identical spherical particles. Further on, it is assumed that growth controlled by diffusion in the bulk with a composition-independent effective diffusion coefficient; also volume changes across the solid solutions are neglected. In the following, the Wert-Zener model will be applied to the formation of the iron-rich precipitate in the sample of composition $x = 0.5$. The sample possesses an estimated density of nuclei of the hematite-type phase of about $n = 1{\cdot}10^{17}$ cm^{-3} and, thus, fulfils best the condition for diluted particles of all our samples. The latter value has been derived from $n = \frac{x-x'}{x''\cdot\left(\frac{4}{3}\right)\pi R_\infty^3}$ for spherical precipitate particles of radius $R_\infty = 7$ nm where R_∞ has been determined from the experimental particle size L_w (Table I, $x = 0.5$) by setting $R_\infty \approx L_w/2$ and by using solubility limits of $x' = 0.2$ and $x'' = 1.8$ in accord with our above findings. According to Wert and Zener, the time-dependent radius of the precipitate particles is determined by

$$RdR = D \cdot \left(\frac{x - x'}{x'' - x'}\right) \cdot (1 - W(t))dt \qquad (2)$$

where W represents the fraction of precipitated material. For large values of W, which is the case of present interest, an asymptotic solution of W is given by $W(t) = 1 - 2\exp\left(-\frac{3t}{2\tau}\right)$ with the parameter τ defined by $\tau^{-1} = D\left[\frac{48\pi^2(x-x')}{x''}\right]^{1/3} n^{2/3}$.[49,50]

Figure 6 shows the time-dependent radius of a precipitate particle according to Eq. (2) for different effective diffusion coefficients D. As seen, for a diffusion coefficient ($D_1 = 8 \cdot 10^{-15}$ cm^2/s) of the magnitude of the tracer diffusion coefficient of ^{26}Al in Al_2O_3 at 1250°C,[47] the full size of the particles ($R_\infty = 7$ nm) is not reached in any reasonable time. However, already a diffusion coefficient of only one order of magnitude larger causes the precipitates to grow almost to the final radius within about 10 s. It is highly likely that the rate-determining diffusion

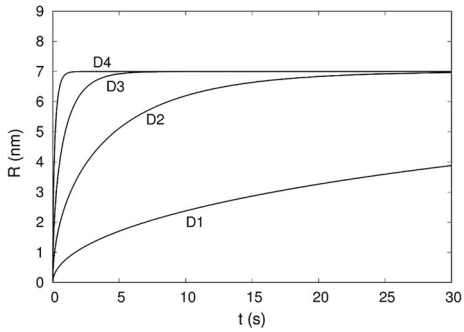

Fig. 6. Time-dependent growth of spherical precipitate particles for different effective diffusion coefficients in the framework of the Wert-Zener theory. Calculations of $R(t)$ for the sample with $x = 0.5$ and for effective diffusion coefficients of $D_1 = 8{\cdot}10^{-15}$ cm^2/s, $D_2 = 1{\cdot}10^{-13}$ cm^2/s, $D_3 = 5{\cdot}10^{-13}$ cm^2/s, and $D_4 = 2.5{\cdot}10^{-12}$ cm^2/s.

of Al in iron containing solid solutions is significantly enhanced in comparison to that in pure Al_2O_3. Therefore, it appears quite conceivable that cation transport in combustion synthesis after ignition is sufficiently rapid at peak-temperatures to create nanophases which are at equilibrium—or very close to it. Finally, it also appears worth mentioning that the temperature of about 1250°C represents an effective quenching temperature and that during combustion even higher temperatures may have been reached.

CONCLUSIONS

X-ray diffraction and Mössbauer spectroscopy analysis of combustion-synthesized Ag/$Fe_xAl_{2-x}O_3$ materials ($0.5 \le x \le 2$) revealed the formation of multi-phase nanocomposites consisting for $x < 2$ of silver metal and two corundum-type $Fe_xAl_{2-x}O_3$ phases. One of the latter phases possesses high alumina content whereas the other represents a hematite-rich phase. Mössbauer signal intensities of samples with $x = 0.5$, 1.0, and 1.5 could consistently be explained by coexistence of phases of approximate composition $Fe_{0.2}Al_{1.8}O_3$ and $Fe_{1.8}Al_{0.2}O_3$, which closely corresponds to the thermodynamic equilibrium phase diagram of Fe_2O_3-Al_2O_3 at about 1250°C. Obviously, this resulted from the combustion synthesis using urea as combustion fuel of the reactive gel prepared from the component nitrates. In particular, it is considered to be due to the combined effect of high temperatures reached due to ignition of the reactive gel and the presence of iron oxide providing preferred nucleation sites effectively limiting the growth of grains to the nanoscale. At the same time, it is concluded that cation transport must have been sufficiently rapid to achieve phase separation with close to equilibrium cation concentrations. The latter conclusion is supported by modeling growth kinetics of the precipitate particles in the framework of the Wert-Zener model of diffusion-controlled growth. Finally, the Mössbauer spectra reveal line shape changes for the samples with $x < 2$, which are characteristic for the

onset of superparamagnetic behavior. This confirms that grain growth was effectively controlled and limited and that the average size of the crystallites of the iron-rich phase is less than 20 nm which is in perfect agreement with results deduced from XRD lines broadening.

ACKNOWLEDGMENTS

We would like to thank Prof. Klaus-Dieter Becker, Institute of Physical and Theoretical Chemistry, Technische Universität Germany for providing the Mössbauer measurements.

REFERENCES

1. G. Bantsis, M. Betsiou, A. Bourliva, T. Yioultsis, and C. Sikalidis, *Ceram. Int.* 38, 721 (2012).
2. S. Bhagwat, S. Joshi, S.B. Ogale, G. Marest, A. Benyagoub, N. Mancoffre, and F. Thimon, *J. Appl. Phys.* 79, 4141 (1996).
3. W. Wang, W. Liu, X. Yang, and Z. Xie, *Ceram. Int.* 38, 2851 (2012).
4. L. Zhou, W. Zhou, J. Su, F. Luo, and D. Zhu, *Ceram. Int.* 38, 1077 (2012).
5. S. Bid, A. Banerjee, S. Kumar, S.K. Pradhan, U. De, and D. Banerjee, *J. Alloys Compd.* 326, 292 (2001).
6. R.J. Willey, H. Lai, and J.B. Peri, *J. Catal.* 130, 319 (1991).
7. M. Niwa, K. Yagi, and Y. Murakami, *Bull. Chem. Soc. Jpn* 54, 975 (1981).
8. A. Lycourghiotis and D. Vattis, *React. Kinet. Catal. Lett.* 18, 377 (1981).
9. V.I. Kuznetsov, E.N. Yurchenko, M.T. Protasova, E.A. Taraban, O.P. Krivoruchko, and R.A. Buyanov, *Phys. Status Solidi (a)* 113, 359 (1989).
10. M.C. Prieto, J.M.G. Amores, V.S. Escribano, and G. Busca, *J. Mater. Chem.* 4, 1123 (1994).
11. J.L. McArdle and G.L. Messing, *J. Am. Ceram. Soc.* 76, 214 (1993).
12. L.F. Cótica, A. Paesano Jr, S.C. Zanatta, S.N. de Medeiros, and J.B.M. da Cunha, *J. Alloys Compd.* 413, 265 (2006).
13. P. Tartaj and J. Tartaj, *Acta Mater.* 50, 5 (2002).
14. J. Kákoš, L. Bača, P. Veis, and L. Pach, *J. Sol-Gel. Sci. Technol.* 21, 167 (2001).
15. International Centre for Diffraction Data, PDF 10-173 (α-Al_2O_3) and PDF 13-534 (α-Fe_2O_3).
16. J.F. Bengoaa, A.M. Alvareza, A.E. Bianchib, G. Punteb, R.E. Vandenberghec, R.C. Mercaderb, and S.G. Marchettia, *Mat. Chem. Phys.* 123, 191 (2010).
17. N. Mimura and M. Saito, *Catal. Today* 55, 173 (2000).
18. G. Giecko, T. Borowiecki, W. Gac, and J. Kruk, *Catal. Today* 137, 403 (2008).
19. N.R.E. Radwan, E.A. El-Sharkawy, and A.M. Youssef, *Appl. Catal. A* 281, 93 (2005).
20. S. Kobayashi, S. Kaneko, M. Ohshima, H. Kurokawa, and H. Miura, *Appl. Catal. A* 417–418, 306 (2012).
21. B.M. Abu-Zied, *Appl. Catal. A* 334, 234 (2008).
22. G. Longworth: in Mössbauer Spectroscopy Applied to Inorganic Chemistry, G.J. Long (Ed.), Vol. I, p. 43. Plenum Press, New York (1984).
23. K. Lagarec, D.G. Rancourt, Recoil-Mössbauer spectral analysis software for windows version 1.02, Department of Physics, University of Ottawa, (1998).
24. W. Gessner, *Anorg. Allgem Chemie* 360, 247 (1968).
25. T. A. Taha, S., Elrabaie, M. T. Attia, J. Mater. Sci. Mater. Electron., 29(21), 18493 (2018).
26. M.H. Yao, R.J. Baird, F.W. Kunz, and T.E. Hoost, *J. Catal.* 166, 67 (1997).
27. S. Zhan, D. Chen, X. Jiao, and S. Liu, *J. Colloid Interface Sci.* 308, 265 (2007).
28. S. Krehula and S. Musić, *J. Alloys Compd.* 416, 284 (2006).
29. B.T. Poe, P.F. McMillan, C.A. Angell, and R.K. Sato, *Chem. Geol.* 96, 333 (1992).
30. M. Okuno, N. Zotov, M. Schmücker, H. Schneider, and J. Non-Cryst, *Solids* 351, 1032 (2005).
31. M. Ristić, E. De Grave, S. Musić, S. Popović, and Z. Orehovec, *J. Mol. Struct.* 834–836, 454 (2007).
32. S. Musić, I. Czakó-Nagy, I. Salaj-Obelić, and N. Ljubešić, *Mater. Lett.* 32, 301 (1997).
33. J.E. Iglesias and C.J. Serna, *Miner. Petrogr. Acta* 29A, 363 (1985).
34. M. Ristić and S. Musić, *J. Alloys Compd.* 425, 384 (2006).
35. Y. Wang, A. Muramatsu, and T. Sugimoto, *Colloid Surf. A: Physicochem. Eng. Aspects* 134, 281 (1998).
36. F. Menil, *J. Phys. Chem. Solids* 46, 763 (1985).
37. O.C. Kistner and A.W. Sunyar, *Phys. Rev. Lett.* 4, 412 (1960).
38. A. Muan and C.L. Gee, *J. Am. Ceram. Soc.* 39, 207 (1956).
39. F.A. Elrefaie and W.W. Smeltzer, *Metall. Trans. B* 14, 85 (1983).
40. R. Hansson, P.C. Hayes, and E. Jak, *Metall. Mater. Trans.* 35B, 633 (2004).
41. M.A. Rhamdhani, T. Hidayat, P.C. Hayes, and E. Jak, *Metall. Mater. Trans.* 40B, 25 (2009).
42. A.K. Ladavos and T.V. Bakas, *React. Kinet. Catal. Lett.* 73, 223 (2001).
43. A. Cordier, A. Peigney, E. De Grave, E. Flahaut, and C. Laurent, *J. Eur. Ceram. Soc.* 26, 3099 (2006).
44. L.F. Cotica, S.C. Zanatta, M.A. Rocha, I.A. Santos, A. Paesano Jr, J.B.M. da Cunha, and B. Hallouche, *J. Appl. Phys.* 95, 1307 (2004).
45. M. Liu, H. Li, L. Xiao, W. Yu, Y. Lu, and Z. Zhao, *J. Magn. Magn. Mater.* 294, 294 (2005).
46. W. Kündig, H. Bömmel, G. Constabaris, and R.H. Lindquist, *Phys. Rev.* 142, 327 (1966).
47. P. Fielitz, G. Borchardt, S. Ganschow, and R. Bertram, *Defect Diffusion Forum* 323–325, 75 (2012).
48. K. Hoshino and N.L. Peterson, *J. Phys. Chem. Solids* 46, 1247 (1985).
49. C. Wert and C. Zener, *J. Appl. Phys.* 21, 5 (1950).
50. R.J. Borg, G.J. Dienes, An Introduction to Solid State Diffusion, Academic Press Inc., Boston, Chap. XII, (1988).